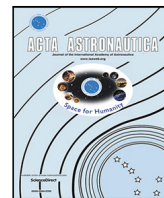




Contents lists available at ScienceDirect

Acta Astronautica

journal homepage: [www.elsevier.com/locate/actaastro](http://www.elsevier.com/locate/actaastro)

## Development of a deployable Synthetic Aperture Radar antenna for a nanosatellite conceptual design

Annalisa Tresoldi <sup>a,\*</sup>, Jason Shore <sup>a</sup>, Andrew C.M. Austin <sup>b</sup>, Guglielmo S. Aglietti <sup>a</sup>

<sup>a</sup> Te Pūnaha Ātea - Space Institute, University of Auckland, Auckland, 1010, New Zealand

<sup>b</sup> Department of Electrical, Computer, and Software Engineering, University of Auckland, Auckland, 1010, New Zealand

### ARTICLE INFO

#### Keywords:

Deployable antenna  
SAR  
CubeSat  
High Strain Composite  
Ploy region

### ABSTRACT

For a real-time maritime surveillance application in the extended territorial waters of New Zealand, this work aims to develop a viable concept design for a deployable Synthetic Aperture Radar (SAR) antenna to fit in a CubeSat design space. To trade off a large antenna aperture, which is essential to enhance SAR performance, and a high packaging efficiency, potentially  $\leq 12U$ , a 4 m x 0.3 m reflectarray with a stiff-and-flexible and novel passive deployable system is selected as the most promising solution for this application. A High Strain Composite (HSC) structure with a shallow “tape-measure” inspired shape is presented to support the SAR reflectarray and compactly stow it through a rollable deployment system. The release of the elastic energy stored in the coiled structure will enable the deployment, and the structural stiffness will be provided by a boundary condition that maintains the naturally curved cross-section during stowage. With this design constraint, the transition zone (ploy region) that develops between the stowed and deployed state may significantly impact the stowage capabilities. The elastic behaviour of the structure will be analytically studied in terms of the change of curvatures and bending stiffness as they dominate the deformed shape in the coiling process. Existing analytical models that predict the ploy regions are considered to estimate the natural ploy length and the equivalent coil diameter. Finite Element (FE) models are developed to compare the analytical models and explore the stress field generated within the ploy region when the length of this region is forced to be shorter than the natural ploy length. FE model observations and data are also used to improve the analytical model that describes the deformed shape by imposing non-uniform boundary conditions on the curvatures’ field distribution within the ploy region.

### Abbreviations

AOCS	Attitude Orbit Control System
CFRP	Carbon Fibre Reinforced Polymer
DOF	Degree Of Freedom
FD	Finite Different
FE	Finite Element
FEM	Finite Element Model
HGDA	High Gain Deployable Antenna
HSC	High Strain Composite
RF	Radio Frequency
SAR	Synthetic Aperture Radar

### 1. Introduction

SAR technology has become one of the most powerful means of Earth Observation. The capability of radar sensors to monitor relevant phenomena on Earth (e.g., rapid disaster response, environmental monitoring, crop and ship detection, coastal ice measurement, etc. [1]) can be enhanced by exploiting the use of CubeSats. Being small and relatively cheap satellites, they represent the most attractive, cost-effective solution to develop radar constellations that, in turn, can provide an improved revisit time [2]. However, the installation of large space instruments on CubeSats is severely constrained by the limited resources available. Low mass and volume constraints require a high stowage efficiency for the launch phase and a reliable deployment process in orbit [3]. Accordingly, due to the complexity, significant payload size and high resource demands, SAR systems are generally not

\* Corresponding author.

E-mail addresses: [atre682@aucklanduni.ac.nz](mailto:atre682@aucklanduni.ac.nz) (A. Tresoldi), [jason.shore@auckland.ac.nz](mailto:jason.shore@auckland.ac.nz) (J. Shore), [a.austin@auckland.ac.nz](mailto:a.austin@auckland.ac.nz) (A.C.M. Austin), [g.aglietti@auckland.ac.nz](mailto:g.aglietti@auckland.ac.nz) (G.S. Aglietti).

<https://doi.org/10.1016/j.actaastro.2023.04.009>

Received 7 December 2022; Received in revised form 8 February 2023; Accepted 3 April 2023

Available online 5 April 2023

0094-5765/© 2023 The Authors. Published by Elsevier Ltd on behalf of IAA. This is an open access article under the CC BY-NC-ND license (<http://creativecommons.org/licenses/by-nc-nd/4.0/>).

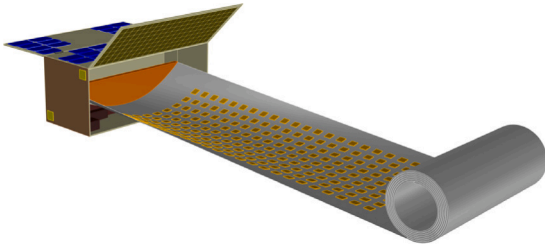


Fig. 1. CAD model of the HSC rolled-up shell deployment process.

installed on nanosatellites (<10 kg), rather state-of-the-art SAR systems are mainly associated with medium/large satellites [4]. Moreover, since SAR performance (i.e., resolution and sensitivity) is directly proportional to the antenna size [5], the requirement of a large SAR antenna compounds the difficulties to fit CubeSats platforms. Most of the High Gain Deployable Antenna (HGDA) have been implemented using active antenna arrays distributed along hinged panel structures, such as the X-band parallel-plate antenna [6], or with large reflector mesh structures that are activated by an antenna array [7]. A potentially lower complex solution in the antenna aperture and Radio Frequency (RF) system is provided by the reflectarray [8], which has been recently investigated in flexible and lightweight membrane structures [9].

Although the higher stowage efficiency compared to more common rigid panel solutions, implementing array cells on thin substrate layers may impact the electrical performance due to membrane wrinkling and creasing after the folding process [10]. Support structures and tensioning systems are required to avoid a low surface accuracy, thus increasing the overall mechanical complexity.

This paper considers a HSC structure with a shallow “tape-measure” [11] inspired shape to overcome these constraints and provide a stiff-and-flexible antenna design potentially adaptable to a 12U CubeSat. The key set of applications for this small-satellite SAR system concern low-power maritime surveillance and Earth subsidence and deformation monitoring. The design concept during deployment is shown in Fig. 1.

HSC booms are generally used to assist the deployment of large space instrumentations by acting as structural support. In fact, after the deployment, these structures recover their curved natural shape increasing the geometric stiffness. Moreover, thanks to the change in the cross-section geometry, HSCs can be easily flattened and rolled on a drum to gain a low stowed volume during launch [12]. By adopting a HSC as a supporting structure, it is proposed that a SAR reflectarray antenna can be implemented on a slightly curved rollable shell and passively deployed through the release of the elastic energy stored in the stowed coiled configuration. It is aimed to develop a novel passive deployment system that avoids the use of active motors, instead providing low mechanical complexity and a low-mass solution.

A key aspect of the HSC design is the root’s boundary condition [13] that, for this application, is maintained curved and fixed, as illustrated in Fig. 1. An example of this type of boundary condition is Roccor’s COBRA system that utilizes a HSC to deploy a solar array system that is bonded to the surface [11]. When the natural shell curvature is rigidly maintained at the root, the self-stiffening capability of the HSC is maximized. However, the transition zone (ploy region) between the flat and curved state may significantly constrain the achievable final stowed volume as it exhibits the highest concentration of stresses in the structure [14].

This paper will present qualitative aspects of the system requirements and a trade-off design process before introducing the preliminary study on the ploy region. The questions that are going to be addressed in this work are:

- Why is a thin and shallow shell design required for this application? Which are the design parameters that can be varied to minimize the final stowed mass and volume?

Table 1  
SAR system design parameters.

Parameters	Symbol	Value	Unit
Average transmit power	$P_{ave}$	< 150	W
Wavelength	$\lambda$	0.03	m
Antenna length	$L_a$	1–4	m
Antenna width	$W_a$	0.3–0.4	m
Look angle	$\Gamma$	20–40	°
Noise figure	F	5	dB
System losses	L	5	dB
$R_x$ bandwidth	$B_r$	100–300	MHz

- Why is a clamped root’s boundary condition a key aspect in the design process? What are the implications for the ploy region?
- Given the system requirements, what design factors impact the ploy length? How well correlated are the FE results with the existing analytical solutions in a free-constraint and enforced state?

## 2. Application-driven SAR system requirements

The SAR satellite design in this study aims to address maritime surveillance in the extended territorial waters of New Zealand. As discussed in previous studies [15]–[16], detection of vessels with a minimum size of 30 m in length and 7 m in width can be performed using significantly lower power levels and reduced antenna size compared to general purpose SAR systems. An antenna width compatible with a 12U CubeSat was considered to build up a preliminary SAR system design for this application, as reported in Table 1.

Initial considerations on the final stowed volume achievable showed that for a maximum length,  $L$ , of 4 m and flattened width of 0.4 m, a thin shell with a thickness,  $t$ , of  $\sim 0.4$  mm could be rolled on a deployment drum in 10 wraps,  $n$ , calculated by using the Archimedean spiral approximation [17]:

$$n = \sqrt{\left(\frac{r_i}{t}\right)^2 + \frac{L}{\pi t}} - \frac{r_i}{t} \quad (1)$$

Considering an initial large coiling radius  $r_i$  of 60 mm, the approximated final volume occupied by the fully coiled shell is  $\sim 0.0053$  m<sup>3</sup>, which is roughly half of the 12U CubeSat space. However, given the stringent volume constraints, limitations on the size and thickness of the shell directly impact the stiffness and strength of the antenna structure. For instance, the deployed SAR antenna requires a resonant frequency above the Attitude Orbit Control System (AOCS) loop rate (assumed 1 Hz) to avoid resonant frequencies. For this purpose, a slightly curved cross-section is used to support and stiffen the deployed state. In addition, it is envisaged to use a high-stiffness root boundary condition in which the natural curvature is maintained fixed during stowage and deployment. Given a curved-clamped edge, the ploy region extension will ultimately prevent the coiled structure from completely coiling, therefore, the coiled region of the structure will be offset from the fixed root, as shown in Fig. 2. Based on the stowage method used, this may impact the final stowed volume occupied by the antenna structure and deployment mechanism.

## 3. Stowage methods overview

The stowage process consists of two subsequential steps: flattening and coiling. Due to the designed root’s boundary condition, the change of the cross-section from the flat/coiled to the curved/fixed state implies the occurrence of an enforced transition zone that needs to be considered in the stowage method design. Two methods are proposed to assess and then optimize the development of the ploy region. The first method positions the fixed edge inside a deployment drum and provides for the use of a rotating mechanism that assists the flattening of the HSC when forced to rotate around the drum, as shown in Fig. 3,

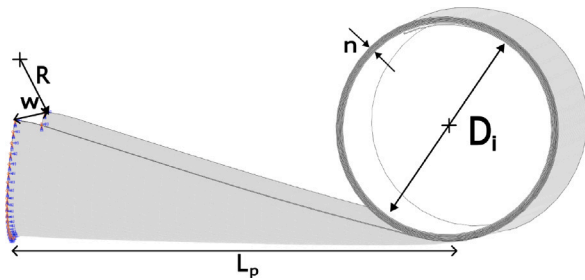


Fig. 2. CAD model of the coiling process with ( $n$ ) number of total wraps, ( $D_i$ ) diameter of the deployment drum, ( $R$ ) initial radius of curvature and ( $L_p$ ) ploy length.

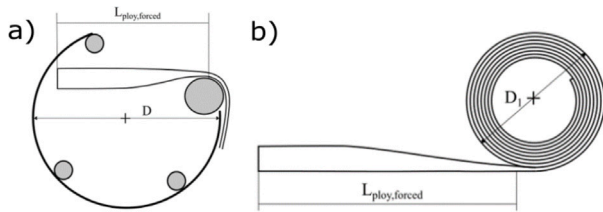


Fig. 3. HSC's curved root boundary condition inside (a) and outside of the deployment drum (b).

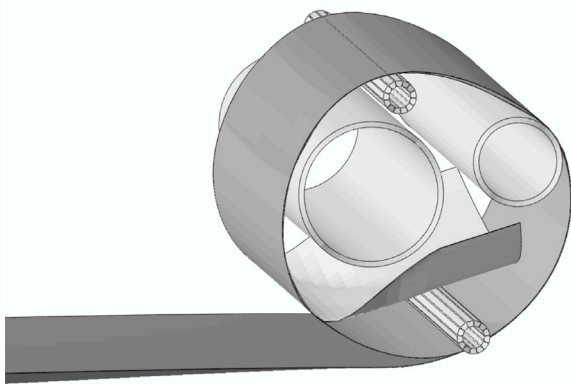


Fig. 4. CAD model of the deployment system of drums with a fully clamped root's boundary condition.

(a). In this case, the shell is flattened close to the fixed edge before rolling, enforcing a ploy region to occur inside the drum. In the second alternate stowage method, the shell is rolled at the free edge after the flattening step, as shown in Figs. 2 and 3, (b).

With this method, the shortened ploy region occurs at the end of the rolling process, and so is outside of the deployment drum.

With configuration (b), the coiling diameter ( $D_i$ ) may be significantly reduced as long as the material failure properties are properly accounted. In addition, this method presents with a higher deployment force if a passive deployment system is used because less friction is involved. However, a larger final stowed volume is expected because the ploy length ( $L_{ploy,forced}$ ) will offset the coiled structure from the bus satellite. On the other hand, a more compact solution could be achieved with the stowage concept (a) at the cost of a larger coiling radius and potential higher mechanical complexity during the deployment. Fig. 4 shows the CAD model of the method of stowage (a) where the clamped boundary condition at the root is captured inside the rotary mechanisms. FE models of both stowage methods are presented later in this paper to highlight and compare the stress field in the ploy region.

In both configurations, the self-deployment of the antenna may cause instabilities on the AOCS due to high deployment velocity. Although design (a) has a higher mechanical complexity, the system of cylindrical rollers that assist the coiling of the antenna will lead to a lower deployment velocity than what is expected in system (b). This is due to the friction generated between the shell's layers and between the shell and the deployer, which will resist the release of the elastic energy stored in the coiled shell. This would, in turn, decrease the self-deployment force, damping out the undesired disturbances that may impact the spacecraft attitude control. Furthermore, the mass of the shell is on the order of 300–600 grams, while the mass of a 12U CubeSat will be on the order of 15–24 kg. This means that the deployment of the shell will only have a small effect on the dynamics of the more massive satellite. Another aspect of the deployment process that may impact the antenna performance is related to the surface deformations that may occur after the unrolling process due to the material relaxation developed in a long-term stowage [18]. However, for the study considered in this work, it is assumed that the deployment process would take place after a few seconds of stowage, enabling us to consider any thermoelastic surface distortions negligible. It is unclear at this stage which mounting option is more efficient, and this will be addressed in future work. In both cases, the HSC design (i.e., curvature subtended angle, thickness, and material selection) will impact the characterization of the ploy region, thus affecting the final stowed volume.

## 4. Design and material selection

### 4.1. Stiffness and foldability

To provide a low-mass and compact stowed solution, the deployment drum diameter and the shell thickness need to be minimized. An exceedingly thick cross-section may prevent the flattening step, and ultimately lead to severe material damage during the coiling process. Generally, a thin and flexible shell is preferred to enable the stowage process on a relatively small deployment drum. However, a trade-off between stiffness and flexibility needs to be considered in the design process. The stiffness of the HSC is driven by the material properties, thickness, and cross-sectional shape of the shell. With the requirement to minimize the thickness, the geometric stiffness may be improved by increasing the initial cross-sectional curvature naturally recovered after deployment. Although a semi-circular cross-section would significantly improve the stiffness properties, some critical factors need to be addressed. First, while a slightly curved surface could be locally approximated to a flat reflectarray with negligible accuracy errors, a deep curved cross-section may complicate the SAR system design due to the geometric curvature. Secondly, since the antenna aperture width is a fixed design parameter for this application, the larger the curvature is the larger the final flattened width has to be. Such a limitation, in turn, will increase the final volume required to stow the antenna. For these qualitative considerations, a slightly curved and thin cross-section is targeted for this preliminary study to simplify the electrical design process and optimize the structural performance.

### 4.2. Trade-off design

Different initial radius of curvature  $R$ , cross-section thicknesses and materials were studied to trade off stiffness and foldability. In the first instance, a reasonable range of subtended angles  $\beta$  for shallow shells was considered between  $60^\circ$  and  $120^\circ$ , as reported in Table 2. As previously noticed, the arc length  $b$  increases with the subtended angle for a given antenna aperture width  $w$ , gaining geometric stiffness at the cost of a final larger flattened width. To define the optimal deployed state design, a linear-perturbation eigenvalue natural frequency analysis was conducted in ABAQUS using SR4 shell elements. For each geometry selected in the trade-off study, the shell has a length of 4 m

**Table 2**  
Shell geometries trade-off study.

Design parameters				
b [m]	0.35	0.37	0.38	0.4
w [m]	0.33	0.33	0.33	0.33
L [m]	4	4	4	4
R [m]	0.33	0.23	0.21	0.19
$\beta$ [°]	60	90	100	120
Cross-section				

**Table 3**  
Laminate layup.

	Thickness [mm]	Layup
#A	0.285	[±45°/0°/±45°]
#B	0.37	[±45°/0°/0°/±45°]
#C	0.425	[±45°/±45°/0°/±45°/±45°]



**Fig. 5.** Deployed frequency analysis of the shell with a boundary condition fixed in the 6 Degree Of Freedom (DOF).

and a cross-sectional chord of 0.33 m. Like in the COBRA system [11], the shell is constrained with a fully fixed boundary condition at the root, while the tip edge is free, as shown in Fig. 5. In [11], a double beam system that is tied at the tip is also studied showing improved stiffness performance than the single beam geometry. However, a single curved shell is preferable for this application because any geometric gaps or discontinuities may impact the electrical performance and will complicate the SAR design.

In addition, operating as the substrate for a reflectarray, a low RF-loss dielectric material is required for the HSC shell. A glass fibre composite is preferred to a Carbon Fibre Reinforced Polymer (CFRP) to ensure lower conductive properties, which will avoid having a detrimental impact on the electrical performance.

It is envisaged that the reflectarray body will consist of a thin glass fibre laminate covered by two layers of metallization to create the desired microwave phase-shifting properties on to the surface. With reference to [17] unidirectional S-2 Glass and plain weave AstroQuartz materials were selected for this preliminary study because they are commonly used in thin-ply composite boom applications. As reported in Table 3, three layup configurations with different fibres orientation were considered in the trade-off study to strike a balance between the deployment force and thickness. As widely investigated in the literature and tested in [19], fibre angles equal to 0° increase the deployment energy while the outer woven layers with a 45° angle ease the rollability.

The modal analysis was conducted for all the shell geometries and layup configurations, showing a similar structural response. Assuming laminate #B as baseline layup, Fig. 6 shows that the first two natural frequencies present with a torsional and a bending mode shape, respectively. These mode shapes are representative of all the cross-sections and thicknesses studied.

Fig. 7 shows the frequency analysis results for each geometry and laminate investigated. It can be noticed that the lowest natural frequency is below 1 Hz for subtended angles below 90° for all the layups proposed for this application. On the other hand, all the laminates

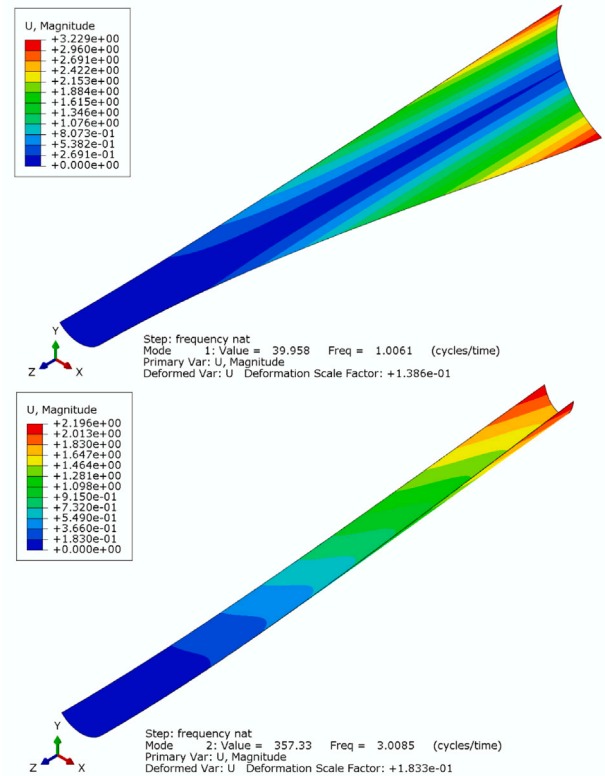


**Fig. 6.** Torsional (top) and Bending (bottom) mode shapes for a shell geometry of  $0.36 \times 4$  m,  $R = 0.23$  m.

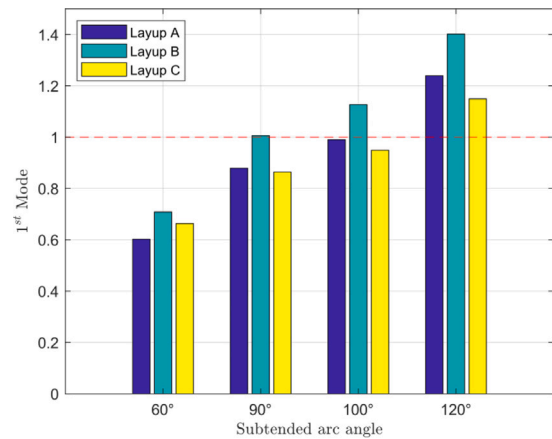


**Fig. 7.** Natural frequency analysis.

with large curvatures performed well due to the improved stiffness properties. Although layup #A and #C may increase the foldability of the shell thanks to more ±45° outer plies in the laminate, they would provide the required structural stiffness only at the largest subtended angle. Such a choice would increase the final stowed volume required. Therefore, layup #B was selected as the baseline laminate because it showed the best results at the shallowest curvatures with a reasonable thickness, which is comparable with the COBRA system [11]. The curvature that subtends the 90° angle will be considered for the design process to develop the FE models and investigate the deformed shape during the coiling process.

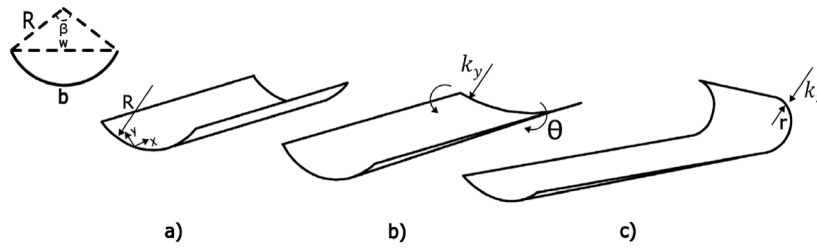


Fig. 8. Flattening and coiling steps with the change in the transverse curvature (b), and longitudinal curvature (c) of the undeformed state (a).

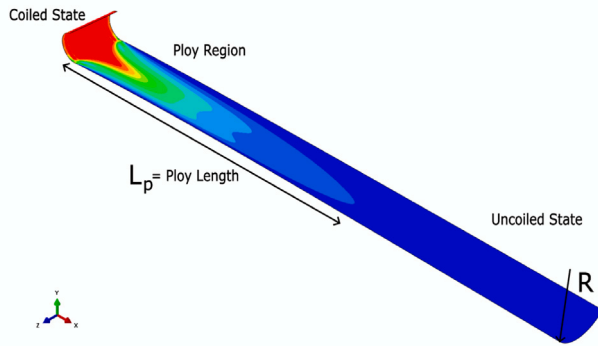


Fig. 9. Ploy region occurrence during the transition from the flat to the uncoiled state.

## 5. Ploy length characterization

To optimize the stowage process and to fit inside a 12U CubeSat platform, the extension of the ploy region in the HSC deformed shape is a crucial point in this feasibility study. As investigated in [20], for high-strain composite parts, the prediction of the natural ploy length is built on relatively recent analytical solutions developed by Yang et al. [14] in 2018 and Seffen et al. [21]–[22] in 2019. While Yang et al. used a strain energy minimization method to estimate the ploy length, Seffen et al. proposed a closed-form solution to quantify it directly. In the case of Yang et al. the strain energy along the ploy region is governed only by the bending deformations that occur due to the change in curvatures in the coiled and uncoiled zone that are bounded by the flat state. By approaching the deployed state, the strain energy increases asymptotically, and the cut-off point to estimate the ploy length ( $L_2$ ) is approximately 5% of the maximum value ( $U_{max}$ ). The strain energy stored from the flat to the uncoiled zone, for an initial transverse curvature  $k_0$ , arc length  $l$  and flexural stiffness terms  $D_{22}$ ,  $D_{12}$  and  $D_{66}$ , is given as:

$$U = \sum_{n=1}^{\infty} \frac{D_{22}l}{8\beta\gamma} [c_3^2(1 - e^{-2\beta\gamma L_2}) - c_4^2(1 - e^{2\beta\gamma L_2}) + 4\beta\gamma c_3 c_4 L_2] + \sum_{n=1}^{\infty} \frac{D_{66}l\beta}{8\gamma} [c_3^2(1 - 4e^{-\beta\gamma L_2} + 3e^{-2\beta\gamma L_2} + 2\beta\gamma L_2 e^{-2\beta\gamma L_2}) + c_4^2(-1 + 4e^{\beta\gamma L_2} - 3e^{2\beta\gamma L_2} + 2\beta\gamma L_2 e^{2\beta\gamma L_2}) - 4c_3 c_4(2\beta\gamma L_2 - e^{\beta\gamma L_2} + e^{-\beta\gamma L_2})] \quad (2)$$

where:

$$\beta = \sqrt{\frac{D_{22}}{D_{12} + 2D_{66}}}$$

$$\gamma = \frac{(2n-1)\pi}{l}$$

$$c_3 = -\frac{4k_0(-1)^{n-1}e^{\beta\gamma L_2}}{(2n-1)\pi e^{\beta\gamma L_2} - e^{-\beta\gamma L_2}}$$

$$c_4 = \frac{4k_0(-1)^{n-1}e^{-\beta\gamma L_2}}{(2n-1)\pi e^{\beta\gamma L_2} - e^{-\beta\gamma L_2}}$$

Seffen et al. relying on solutions developed by Rimrott et al. for isotropic rollable STEMs [23], embedded the in-plane stretching energy of the ploy region in the strain energy calculation by expressing it in terms of curvatures. From their studies on folded bistable tape-springs in [22], they reported the asymptotic change in curvature along the ploy region by adding a numerical factor to the ploy length formulation:

$$L_{ploy} = \frac{b^2}{\pi} \left[ \frac{1 - \nu^2/\xi}{120\xi} \right]^{1/4} \sqrt{\frac{1}{Rt}} \quad (3)$$

where  $b$  is the flattened width,  $\xi = E_y/E_x$  the orthotropic stiffness ratio,  $\nu$  the Poisson's ratio,  $R$  the initial cross-sectional radius, and  $t$  the laminate thickness. In [21], Seffen et al. proposed another formulation of the ploy length that overestimates the end of the region by providing an “absolute” estimate of the ploy distance that results in a more conservative value.

$$L_{ploy} = \frac{b^2}{\sqrt{70}} \left[ \frac{1}{\xi} \right]^{1/4} \sqrt{\frac{1}{Rt}} \quad (4)$$

In this paper, these equations are used to compare the natural ploy length results of the shell geometries investigated against the Finite Element Model (FEM). These lengths are used to set the upper bound diameter of the deployment drum to coil the HSC.

## 6. Transverse curvature and ploy length

As introduced above, Yang's strain energy formulation is expressed in terms of bending stiffness and change of curvatures. When the HSC is flattened at the free edge, it faces a change in the transverse curvature ( $k_y = k_2$ ) from the natural curvature  $k_0 = 1/R$  to 0, as shown in Fig. 8, (b). By giving a coiling radius  $r$ , the longitudinal curvature ( $k_x = k_1$ ) increases from 0 to  $K_0 = 1/r$ , as shown in Fig. 8, (c). The extension of the ploy length, which is relevant for this study, concerns the part of the shell that extends from the flat to the uncoiled state, as shown in Fig. 9.

This region is governed by a change of the  $k_2$  expressed by a second order partial differential equation in [14], while  $k_1$  is assumed to be zero:

$$\frac{\partial^2 k_2}{\delta x^2} + \beta^2 \frac{\partial^2 k_2}{\delta y^2} = 0 \quad (5)$$

As in Yang's study, by superimposing uniform boundary conditions, Eq. (5) was numerically resolved with a Finite Different (FD) method [24] to calculate the curvature distribution along the centreline of the ploy region and compare the results with the FE model, as shown in Fig. 10. The boundary condition for  $k_2$  was set zero at the coiled edge and  $k_0$  on the other edges. For this FE model, the initial radius of curvature was set at 0.23 m, which was selected in Section 4.2. In Fig. 10, it can be noticed that  $k_2$  increases asymptotically until the complete recovery of the initial curvature, while  $k_1$  drops rapidly to 0 and remains constant in the uncoiled zone, as predicted

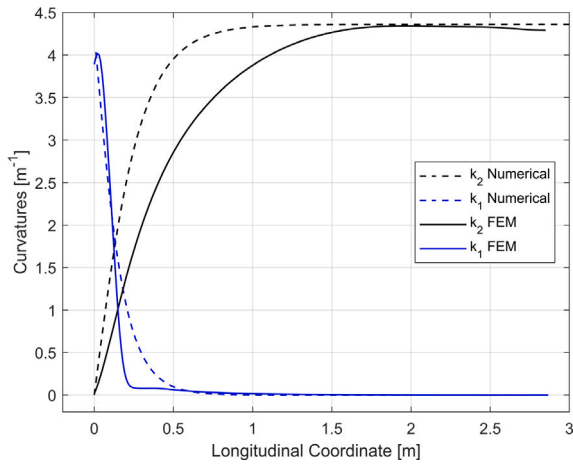


Fig. 10. Curvature distributions along the longitudinal coordinate of the ploy region.

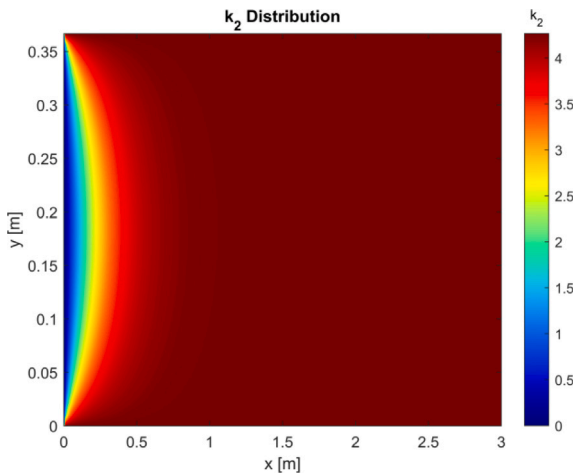


Fig. 11. Contour plot of the transverse curvature from the flat to the uncoiled state.

by the analytical solution. The  $k_1$  curve was calculated with the same numerical approach for a given coiled curvature  $K_0 = k_0$ . In general, the curves show a similar trend between the analytical and FE results. However, there is faster growth of the analytical  $k_2$  when compared to the FE curve, which could be due to the assumed constant boundary conditions and by neglecting  $k_1$  in this region.

The contour plot in Fig. 11, shows the  $k_2$  development derived from Eq. (5) with the imposed uniform boundary conditions. These discrepancies in the rate of the curvature recovery may also be related to the in-plane stretching strains that are neglected in this analytical model. The affect and importance of the assumed boundary conditions is investigated later in the paper.

## 7. FE model

Based on results from Section 4.2, the composite laminate #B in Table 3 is considered for the shell FE model. For the simplicity of the deployment mechanism, the FE model that considers the method of stowage (b) in Fig. 3 is described here and used for the following study. Given an initial radius of curvature of 0.23 m and subtended angle of  $90^\circ$ , the shell was modelled in the deployed state of 4 m length. ABAQUS/Standard 2022 was used to set a dynamic model of the coiling process. One edge of the shell was constrained in the 6 DOF, the opposite edge was free.

Table 4

Analytical vs. FE ploy length prediction.

Natural ploy length $L_{ploy}$				
$\beta$ [°]	Eq. (2)	Eq. (3)	Eq. (4)	FEM
60	0.98 m	1.14 m	1.65 m	1.14 m
90	1.04 m	1.53 m	2.21 m	1.40 m
100	1.07 m	1.67 m	2.42 m	1.72 m
120	1.13 m	2.00 m	2.90 m	1.88 m

The model consists of three steps where the boundary conditions and displacements were set to flatten the free edge of the shell and subsequently roll it.

SR4 shell elements with an element size of 0.01 m (14400 elements) were used to mesh the shell. A cylindrical deployment drum was also modelled as a discrete rigid body to enable the coiling with a diameter of 0.2 m. A general contact interaction was used with properties of “Hard” contact in the normal behaviour and a penalty of 0.1 for the tangential behaviour. The coiling process of the FE model is shown in Fig. 12. In the first step, the free lateral edges were flattened by rotational displacements to extend the shell width (Fig. 12, (a)). In the second step, the contact between the HSC shell and deployment drum was established by enforcing a vertical displacement of the drum (Fig. 12, (b)). In the last step, a rotational displacement was applied to the deployment drum to coil the shell (Fig. 12, (c)). The natural ploy length in this model was captured based on the transverse curvature distribution along the longitudinal centreline from the flat to the uncoiled state. The section curvatures (SK in ABAQUS) were requested as output of the simulation and the end of the ploy region was determined at the coordinate where the change in curvature reached the 95% of the uncoiled state.

Being that the uncoiled edge was constrained in all the DoF, a sufficiently long shell was modelled to capture the natural recovery of the initial curvature. The ploy lengths were calculated for all the shell geometries described in Table 2 based on the change in the transverse curvature, as shown in Fig. 13. The dots along the curves refer to the ploy distance estimations. The FE ploy distances are summarized and compared with the analytical values in Table 4.

It can be seen that there is a good correspondence of results between the ploy length predicted by Seffen et al. in Eq. (3) and the finite element data. In general, an overestimated value of  $L_{ploy}$  is instead provided by Seffen et al. with Eq. (4).

These estimations are consistent with the assumptions that describe the asymptotic decay nature of this region and set the cut-off points to determine the ploy distance. Meanwhile, in the case of Yang et al. the analytical ploy lengths were extracted from each zone by using  $n = 10$  terms in the summation. The lengths of the two zones were then summed to get the final ploy length. These results generally show lower values than the other methods and FE predictions. This underestimation may be justified by assuming that the in-plane strain was neglected in Yang et al. analytical model. Instead, strains from the FE model that develop along the ploy length are observable in Fig. 14. Strain data was extracted in the X direction of the outer surfaces of the shells studied. In general, strains show a maximum at the beginning of the ploy region and a quasi-linear drop along the length until the shape recovery. The contour plot of the maximum principal strains is also shown in Fig. 15 to capture the strain distribution. Similar trends of strains can be noticed in a previous study of folded bistable composite tape-spring [25].

### 7.1. Discussion of results and limitations

The ploy distances from the FE model have been derived from a state that is as free as possible so that the boundary conditions did not impact the solution. For this reason, these results relate to the ploy region that naturally develops along the deployed state, which is not

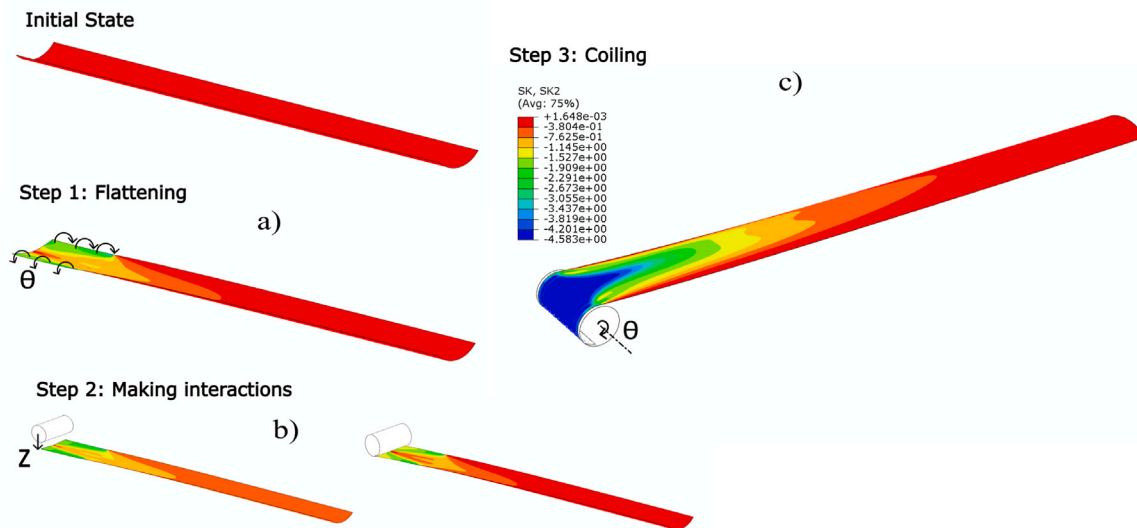


Fig. 12. Coiling process of the FE model: flattening (a), making interaction (b) and coiling (c).

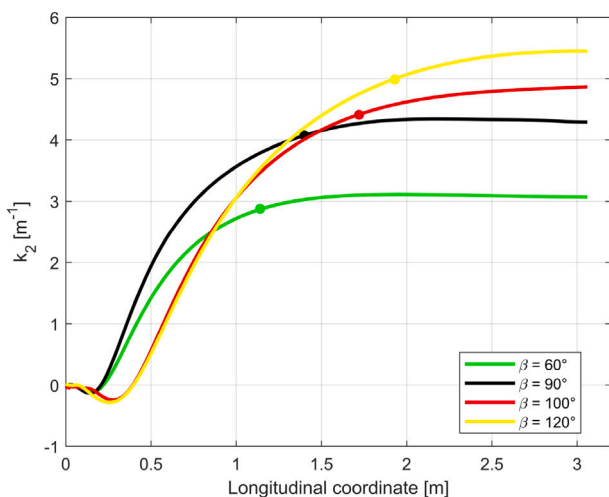


Fig. 13. FE transverse curvature distribution for all the shell geometries with the relative ploy length calculation.

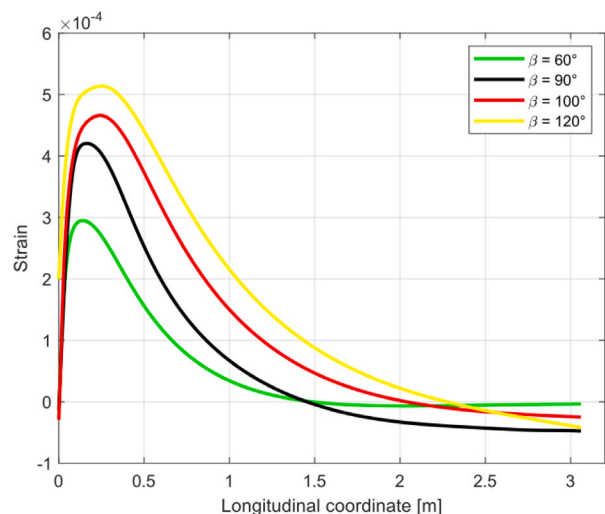


Fig. 14. FE strains distribution in X-direction for the shell geometries along the ploy length.

representative of the actual ploy length expected from the proposed system shown in Fig. 3, (b). However, these results do give an upper bound diameter of the deployment drum that can be used to roll the HSC. As expected, such values are much larger than the diameter of the deployment drum that would be required for a low-stowed volume solution. To obtain a tighter system and reduce the coiled diameter of the drum, the transition zone needs to develop closer to the root's boundary condition. By doing so, the ploy region is forced to be shorter, and a reduced ploy length is expected to occur.

In addition, this study gives us insights into which geometric factors may influence the ploy region. In general, in Table 4 and in Fig. 13, it is shown that the change of the initial subtended angle from 60° to 120° affects the ploy region extension. By keeping the antenna aperture width constant for system requirements purposes, the ploy length increases for larger flattened widths due to the proportionality with the subtended angle. In Table 4, it can also be noticed that the ploy distance results are well-correlated for the lowest subtended angle with a range of underestimation (Eq. (2)) and overestimation (Eq. (4)) of the ploy length between the -14% and +44% compared to the length calculated by Eq. (3) and the FE model. However, the solutions diverge for larger subtended angles by an increase of 60% compared to the shortest length estimation. This could be related to the strains involved in recovering the initial curvature. Fig. 14 shows that when the subtended angle is reduced there is less strain in the shell. Therefore, neglecting the strain in the derivation of the analytical model is more justified for these shell geometries. This would naturally lead to a reduced error between the analytical and FE model predictions of the ploy length, which is shown to be true in Table 4. Consequently, a slightly curved cross-section may reduce the stress and strain field of the enforced ploy region during the coiling process.

### 8. Enforced ploy length

FE models for both stowage methods were developed to conduct dynamic analysis of the full coiling process and set initial considerations on the ploy region by data observations. By enforcing the ploy length to develop closer to the root's boundary condition, a distinct stress field distribution develops, which is also commonplace in small tape-spring case studies [26]. Although a significantly wider shell is considered in this study, in Figs. 16 and 17, two localized regions of high stress are captured along with triangular regions in which there is a lower distribution of the stress. This is the structure attempting to minimize the strain energy stored by concentrating the more costly stretching

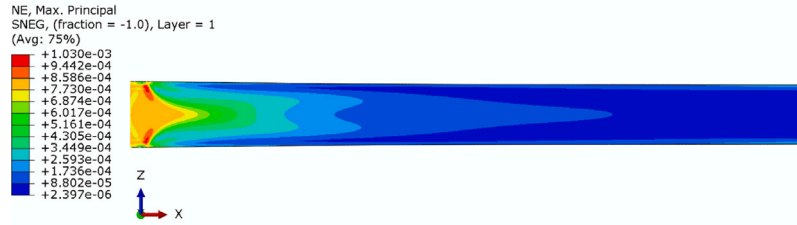


Fig. 15. Maximum principal strain contour.

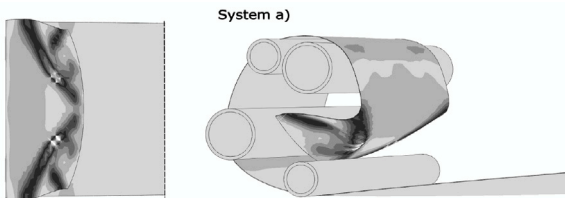


Fig. 16. FE model contour of the ploy region of system (a) with two localized regions of high stress highlighted in black and a triangular region of lower stresses captured in light grey. Bottom view on the left (the drums are omitted), 3D view on the right. (For interpretation of the references to colour in this figure legend, the reader is referred to the web version of this article.)

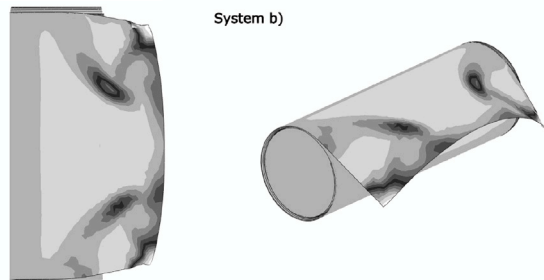


Fig. 17. FE model contour of the ploy region of system (b) with two localized regions of high stress highlighted in black and a triangular region of lower stresses captured in light grey. Bottom view on the left, 3D view on the right. (For interpretation of the references to colour in this figure legend, the reader is referred to the web version of this article.)

Table 5  
Stress comparison in the X and Y directions.

Stress [MPa]	System (a)		System (b)	
	$\sigma_x$	$\sigma_y$	$\sigma_x$	$\sigma_y$
Outer Surface	240	-199	315	-270
Inner Surface	-277	181	-320	206

energy over a smaller area. The first term of comparison between the two methods concerns the maximum stresses that develop in this region. The stresses extracted in the X and Y directions of the composite material for the outer and inner surfaces are compared in Table 5. For a given deployment diameter of 20 cm in system (a) the stresses are shown to be lower both in tension and compression than in system (b), despite a smaller deployment diameter of 12 cm being considered. Indeed, although the structure is coiled in a tighter solution, the stresses localized in the ploy region are shown to be higher. In this comparison, the HSC shell in system (b) was coiled up to 10 cm from the root's fixed edge in order to account for a similar final stowed volume occupied by the coiled structure.

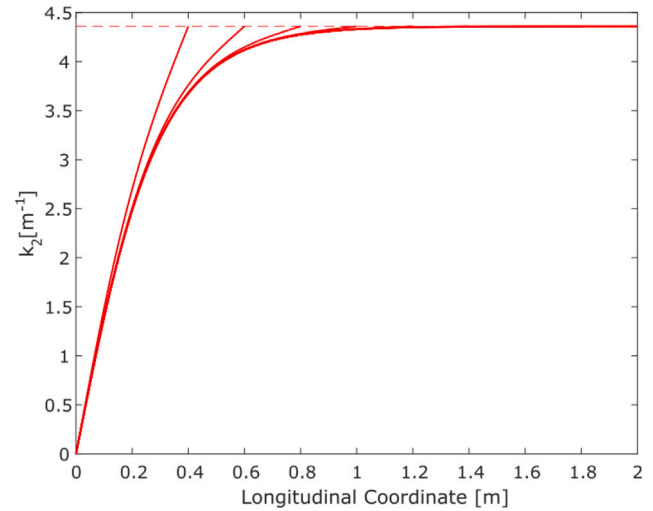


Fig. 18. Change of the transverse curvature at shorter distances to the fixed edge.

In order to select the most efficient method of stowage for this application, these results and a strain energy assessment within the ploy region will be developed in future work. Alongside this work there will be an experimental body of work to validate the FEM results and to derive failure strains for the material.

### 8.1. Non-uniform boundary conditions

Given the full dynamic coiling of the shell by using the system (b), initial observations and FE data on the change of the transverse curvature in the enforced ploy region have been studied. The main objective was to identify the curvature trends from the FEM and consequently improve the analytical model that implements Eq. (5) within an enforced length, which is necessary for the presented application in this paper. Indeed, as the work by Yang et al. [14], by using uniform boundary conditions to describe the field of curvature distribution, the lateral edge deformations that occur during the coiling process are not accounted for because the constant value of  $k_0$  is maintained along the entire edge length. To identify the limitation of this analytical model, in Fig. 18, the transverse curvatures calculated along the centreline with uniform boundary conditions at the edges are compared when a shorter solution length is enforced. As expected, there is a faster recovery of the initial curvature as the coiled shell is closer to the root's boundary condition. This is the shell attempting to break its flat condition unnaturally due to the influence of the imposed root's curvature.

However, although the faster growth of the curves is consistent with the shorter distances, there are no significant changes in the initial part of the curves; rather they show to overlap. In contrast, it is expected that by enforcing the ploy region, the edge deformations increase and ultimately affect the whole  $k_2$  field.

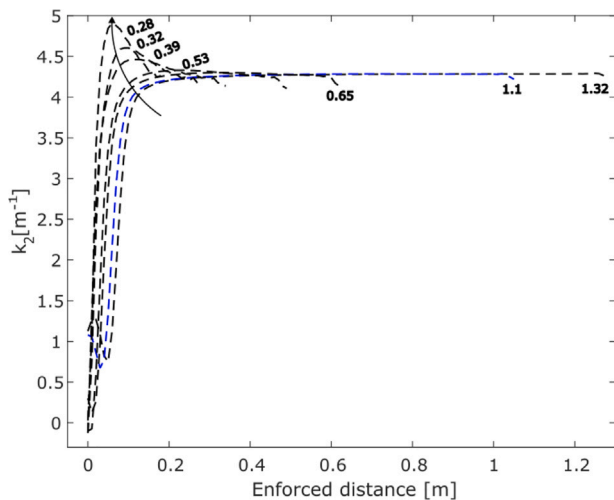


Fig. 19. Change of the transverse curvature along the lateral edges at shorter distances from the fixed edge. Dashed blue line refers to the critical distance  $L^*$ . (For interpretation of the references to colour in this figure legend, the reader is referred to the web version of this article.)

In Fig. 19, such deformation on the lateral edges is reported in terms of  $k_2$ . It can be seen that at enforced distances, the edges of the shell tend to close towards the inside, which is evident from the curvature increasing above the stress-free curvature of  $k_0 = 4.3 \text{ m}^{-1}$ , before re-opening to the imposed value of  $k_0$  at the root.

Such constraints revealed to decrease the analytical model accuracy at reduced ploy distances. In fact, this model is limited to approximate a logarithmic trend of the curve that correlates well the behaviour of  $k_2$  at long distances from the fixed edge. In contrast, at lengths shorter than a critical distance  $L^*$ , FE data on  $k_2$  along the centreline shows a sharp growth change from logarithmic to cubic. To account for this trend, the development of  $k_2$  along the edge at  $L^*$  was approximated by non-uniform boundary conditions. In the first instance, it is assumed that  $k_2$  increases linearly along the edges until 30% of the enforced distance before reaching the constant value of  $k_0$ . The linear and asymptotic increasing at  $L^* = 1.1 \text{ m}$  is highlighted in Fig. 19. These conditions showed to improve the prediction of  $k_2$  along the centreline by reducing the logarithmic power and approximating the FE curve more effectively. Fig. 20 clearly shows the improvement of the analytical model that adopts non-uniform boundary conditions by comparing the results with the FE data and the previous analytical model that has uniform boundary conditions.

It should be noted that such implementation enabled to get a better approximation of the  $k_2$  field of distribution although the stretching deformations have been neglected, as assumed in Eq. (5). For this reason, the assumption that the bending stiffness is predominant in the ploy region is still reasonable. This model has some limitations that will be addressed in future work.

For instance, for shorter distances than  $L^*$ , the boundary conditions need to be further enhanced to adapt to the edge deformations and approximate the cubic growth of  $k_2$  along the length.

## 9. Conclusion and future work

A HSC rollable shell adaptable to the 12U class CubeSat has been developed to provide a new deployable antenna concept that supports a SAR system for a low-power remote sensing application. A preliminary trade-off study on the composite shell geometries and stiffness has been conducted to ascertain the structural and electrical feasibility of this application. A thin glass fibre composite of 0.37 mm is envisaged to be used for a shallow shell that subtends an angle of  $90^\circ$ . This geometry has been shown to have a first mode natural frequency of greater than

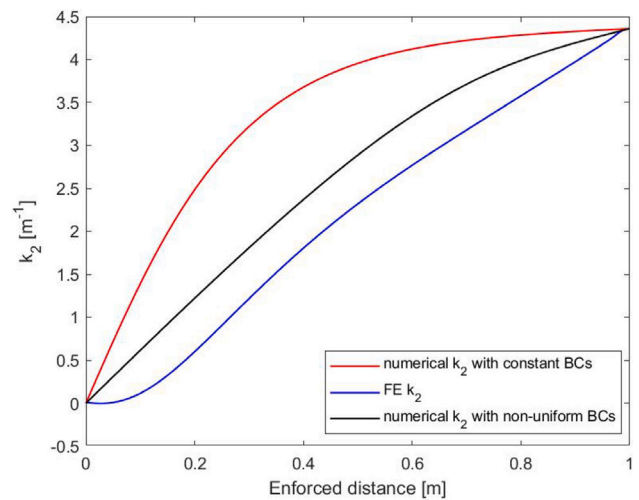


Fig. 20. Comparison between the FE data of the change of the transverse curvature at  $L^*$  with the analytical curves derived from constant and non-uniform boundary conditions at the edges.

1 Hz in the deployed state, which is adequate for this application, and a flattened width of 0.36 m, which can be adapted to a 12U CubeSat side. Two stowage methods have been proposed in which a high-stiffness boundary condition is considered at the shell's root to provide geometric stiffness after the deployment. To minimize the final stowed volume, the ploy length and ploy region have been investigated through a comparison between analytical solutions that estimate the natural ploy length and FE model results based on the change in the transverse curvature. As expected, the well-correlated ploy distances extracted from a free-constraints state have been considered a good starting point that sets the upper bound diameter of the deployment drum to coil the HSC. However, some discrepancies between the analytical model and the FE results were shown, which are due to the assumption that constant boundary conditions are applied to the edges. Such discrepancies were shown to increase when an enforced ploy region was investigated, which is critical for both proposed deployment systems. In the first instance, new non-uniform boundary conditions were established that were shown to improve the approximation of the shortened transverse curvature field. A limitation of this simple boundary condition improvement was identified at the point where the curvature at the edge of the shell closes before opening to the clamped root. Future work plans to include this type of edge deformations so that, at short distances, the analytical model is improved. Strain energy data will be used to extend the study on the ploy region and examine the localized stress distribution. It is also envisaged that the analytical model and the FE results will be validated with experimental work. This work will involve manufacturing the composite shell and conducting tests to assess the ploy region during the coiling process. Furthermore, it is envisaged to conduct deployment testing and shock analysis to assess the deployment velocity and force that may impact the satellite structure. This will help us to characterize the surface shape and the surface deformations that may occur due to the change in the viscoelastic properties of the shell that deploys after a long-term stowage. This will then be related to the performance of the antenna.

## Declaration of competing interest

The authors declare that they have no known competing financial interests or personal relationships that could have appeared to influence the work reported in this paper.

## Acknowledgements

The authors acknowledge the New Zealand TEC Entrepreneurial Universities scheme and the University of Auckland for supporting this work as part of the Auckland Space Institute's activities.

## References

- [1] A. da Silva Curiel, P. Whittaker, R. Bird, A. Haslehurst, P. Nejadi, I. Victoria, A. Cawthorne, C. Underwood, M. Sweeting, Synthetic aperture radar on a nanosatellite - is it possible? in: Proc. of the 12th IAA Symposium on Small Satellites for Earth Observation, Surrey Satellite Technology Ltd., 2019, (Accessed 11/08/22) available at <https://openresearch.surrey.ac.uk/outputs/99513630002346>.
- [2] E. Peral, E. Im, L. Wye, S. Lee, S. Tanelli, Y. Rahmat-Samii, S. Horst, J. Hoffman, S.-H. Yun, T. Imken, D. Hawkins, Radar technologies for earth remote sensing from CubeSat platforms, in: Proceeding of the IEEE, Vol. 106, (3) 2018, pp. 404–418, <http://dx.doi.org/10.1109/JPROC.2018.2793179>.
- [3] G. Aglietti, M. Honeth, S. Gensemer, O. Diegel, Deployable optics for cubesats, in: 33rd Annual Conference on Small Satellites, Utah, No. SSC20-VI-06, 2020, (Accessed 30/01/23) available at <https://digitalcommons.usu.edu/smallsat/2020/all2020/135/>.
- [4] Y. Rahmat-Samii, V. Manohar, M.K. Joshua, For satellites, think small, dream big, IEEE Antennas Propag. Mag. 59 (2) (2017) 22–30, <http://dx.doi.org/10.1109/MAP.2017.2655582>.
- [5] Y. Kim, R.L. Jordan, Spaceborne antennas for planetary exploration, in: William A. Imbriale Book, 2006, <http://dx.doi.org/10.1002/0470052783.ch6>, (Accessed 11/08/2022).
- [6] P.R. Akbar, H. Saito, M. Zhang, J. Hirokawa, M. Ando, Parallel-plate slot array antenna for deployable SAR antenna onboard small satellite, IEEE Trans. Antennas and Propagation 64 (5) (2016) 1661–1671, <http://dx.doi.org/10.1109/TAP.2016.2536164>.
- [7] D. Castelletti, G. Farquharson, C. Stringham, M. Duerschand, D. Eddy, Capella space first operational SAR satellite, in: IEEE International Geoscience and Remote Sensing Symposium IGARSS, 2021, pp. 1483–1486, <http://dx.doi.org/10.1109/IGARSS47720.2021.9554100>.
- [8] J. Huang, Antenna Engineering Handbook, The McGraw-Hill Companies, 2007, (Accessed 25/08/2022) available at <https://www.accessengineeringlibrary.com/content/book/9780071475747>.
- [9] L. Zhi-Quan, Q. Hui, X. Li, S.-L. Yang, Review of large spacecraft deployable membrane antenna structures, Chin. J. Mech. Eng. 30 (2017) 1447–1459, <http://dx.doi.org/10.1007/s10033-017-0198-x>.
- [10] P.A. Warren, J.W. Steinbecj, R.J. Minelli, Large, deployable S-band antenna for a 6U cubesat, in: 29th Annual AIAA/USU Conference on Small Satellites, 2015, (Accessed on: 12/08/2022) available at PM 5.00 - Large, Deployable S-Band Antenna for a 6U CubeSat.pdf.
- [11] D. Turse, L. Adams, K.A. Medina, K. Steele, T. Stern, Design, analysis and testing of a composite beam roll-out array (COBRA) for small satellites, in: AIAA 2019-2024, 2019, <http://dx.doi.org/10.2514/6.2019-2024>.
- [12] B. Davis, D. Turse, W.H. Francis, The deployment of large de-orbit sails utilizing high strain composite booms, in: AIAA 2019-1750, 2019, <http://dx.doi.org/10.2514/6.2019-1750>.
- [13] J. Shore, A. Viquerat, G. Richardson, G. Aglietti, The natural frequency of drum-deployed thin-walled open tubular booms, Thin-Walled Struct. 170 (2022) <http://dx.doi.org/10.1016/j.tws.2021.108650>.
- [14] L. Yang, H. Tan, Z. Cao, Modeling and analysis of the ploy region of bistable composite cylindrical shells, Compos. Struct. 192 (2018) 347–354, <http://dx.doi.org/10.1016/j.compstruct.2018.02.085>.
- [15] J. Krecke, M. Villano, N. Ustalli, A.C.M. Austin, J.E. Cater, G. Krieger, Detecting ships in the New Zealand exclusive economic zone: Requirements for a dedicated SmallSat SAR mission, IEEE J. Sel. Top. Appl. Earth Obs. Remote Sens. 14 (2021) 3162–3169, <http://dx.doi.org/10.1109/JSTARS.2021.3062858>.
- [16] N. Ustalli, G. Krieger, M. Villano, A low-power, ambiguous synthetic aperture radar concept for continuous ship monitoring, IEEE J. Sel. Top. Appl. Earth Obs. Remote Sens. 15 (2022) 1244–1255, <http://dx.doi.org/10.1109/JSTARS.2021.3136935>.
- [17] J.M. Fernandez, Advanced deployable shell-based composite booms for small satellite structural applications including solar sails, in: International Symposium on Solar Sailing, 2017, (Accessed on: 12/08/2022) available at [https://elib.dlr.de/111630/1/Zander\\_AVT-257\\_Belvin\\_NATO\\_CS0\\_Spain\\_Paper.pdf](https://elib.dlr.de/111630/1/Zander_AVT-257_Belvin_NATO_CS0_Spain_Paper.pdf).
- [18] A. Brinkmeyer, S. Pellegrino, P.M. Weaver, Effects of long-term stowage on the deployment of bistable tape springs, J. Appl. Mech. 83 (1) (2015) [https://asmedigitalcollection.asme.org/appliedmechanics/article-pdf/83/1/011008/6082570/jam\\_083\\_01\\_011008.pdf](https://asmedigitalcollection.asme.org/appliedmechanics/article-pdf/83/1/011008/6082570/jam_083_01_011008.pdf).
- [19] J. Ekelöw, Design and manufacturing of thin composite tape springs, (Master's thesis), KTH, School of Engineering Sciences (SCI), Aeronautical and Vehicle Engineering, Aerodynamics, 2014, TRITA-AVE ISSN 1651-7660 2014:84, <http://urn.kb.se/resolve?urn=urn:nbn:se:kth:diva-164296>.
- [20] A.S. Rakow, R. Reedy, Predicting ploy length of high-strain composite slit-tubes and tape-springs, in: AIAA SCITECH 2022 Forum, <http://dx.doi.org/10.2514/6.2022-2266>, <https://arc.aiaa.org/doi/abs/10.2514/6.2022-2266>.
- [21] K.A. Seffen, B. Wang, S.D. Guest, Folded orthotropic tape-springs, J. Mech. Phys. Solids 123 (2019) 138–148, <http://dx.doi.org/10.1016/j.jmps.2018.09.017>.
- [22] B. Wang, K. Seffen, S. Guest, Folding of bistable composite tape-springs, Tech. Rep., University of Cambridge, 2019, <http://dx.doi.org/10.17863/CAM.36403>, (CUED/D-STRUCT/TR.252).
- [23] F.P.J. Rimrott, G. Fritzsche, Fundamentals of STEM mechanics, in: S. Pellegrino, S.D. Guest (Eds.), IUTAM-IASS Symposium on Deployable Structures: Theory and Applications, Springer Netherlands, Dordrecht, 2000, pp. 321–333, [http://dx.doi.org/10.1007/978-94-015-9514-8\\_34](http://dx.doi.org/10.1007/978-94-015-9514-8_34).
- [24] J. Shore, The Stiffness and Stability of Drum-Deployed Tape Springs (Ph.D. thesis), 2021, (Accessed on: 28/08/2022) available at <https://ethos.bl.uk/OrderDetails.do?uin=uk.bl.ethos.847755>.
- [25] B. Wang, K.A. Seffen, S.D. Guest, Folded strains of a bistable composite tape-spring, Int. J. Solids Struct. 233 (2021) 111221, <http://dx.doi.org/10.1016/j.ijsolstr.2021.111221>.
- [26] J. Shore, A. Viquerat, G. Richardson, G. Aglietti, Transition region stress concentrations in clamped tape springs, in: AIAA 2020.1436, 2020, <http://dx.doi.org/10.2514/6.2020-1436>.